Available online at www.sciencedirect.com
ScienceDirect
Journal of the European Ceramic Society 28 (2008) 2451–2457
www.elsevier.com/locate/jeurceramsoc

High-temperature mechanical properties of porous $NaMgF_3$ derived from directionally solidified $NaMgF_3$–NaF eutectics

J. Ramírez-Rico [a,*], A.R. de Arellano-López [a], J. Martínez-Fernández [a], A. Larrea [b], V.M. Orera [b]

[a] *Departamento de Física de la Materia Condensada-ICMSE, Universidad de Sevilla-CSIC, P.O. Box 1065, 41080 Sevilla, Spain*
[b] *Instituto de Ciencia de Materiales de Aragón (C.S.I.C.-Universidad de Zaragoza), C/Pedro Cerbuna 12, 50009 Zaragoza, Spain*

Received 21 February 2008; received in revised form 28 March 2008; accepted 1 April 2008
Available online 14 May 2008

Abstract

Porous $NaMgF_3$ ceramics have been fabricated by leaching a NaF–$NaMgF_3$ eutectic in distilled water, producing $NaMgF_3$ with 53% of connected porosity. The eutectic was fabricated using the Bridgman technique at growth rates of 8, 10 and 15 mm/h. The microstructure and composition of the resulting material has been studied by means of X-ray diffraction and SEM. Compression mechanical tests have been performed at different temperatures up to 750 °C, both in constant strain rate and constant stress loading. The microstructure consists of plate-like grains with cylindrical pores in approximately hexagonal packing. Pores are perpendicular in adjacent grains. The compressive strength is found to be rather independent of growth rate, in the range studied. Small differences can be explained using a minimum solid area (MSA) model and differences in the microstructure. In creep experiments, no steady-state regime was observed. Instead, the strain exhibited a series of accelerations that could be associated with damage propagation.

Keywords: B. Porosity; C. Creep; C. Strength; D. Halides; Eutectics

1. Introduction

Porous ceramics with aligned pores have been the subject of much attention lately, primarily for their potential use as hot gas or molten metal filters, heat exchangers or catalysts support,[1] owing to their low density, good chemical and thermal shock resistance, low-thermal conductivity and dielectric constant. Most work has been done in oxide ceramics, but little in fluoride components. Mechanical failure under compressive stress is one of the critical aspects for application of porous ceramics, as well as the implementation of novel fabrication processes that enable better control on the microstructural features of the material. Several fabrication methods exist, such as the replica technique,[2] the use of fugitive fibers[3,4] or by leaching one of the phases in a composite. For instance, Si/SiC composites can be fabricated using wood precursors and the residual Si can be etched to obtain a porous SiC structure with directionally aligned pores that mimic the wood microstructure.[5] A very important issue in the fabrication of porous ceramics is the design of methods allowing microstructure control, with particular emphasis in pore morphology, size and distribution. The presence of hollow struts and processing-related flaws has a critical impact on the mechanical behavior of porous ceramics, and should be avoided. In some applications aligned pores are desired for good gas transport.

Directional solidification techniques applied to non-metallic materials present several advantages when compared to traditional sintering techniques.[6] For instance, Al_2O_3 based eutectics show enhanced mechanical properties because their microstructure can be tailored by controlling growth conditions.[7] Ceramics for high-temperature fuel cell applications can also be grown, and they exhibit different properties when compared to their sintered counterparts.[7–11] Also, non-oxide eutectics have been fabricated for optical applications.[12,13]

Recently, porous $NaMgF_3$ materials have been fabricated using a modified leaching technique.[14] In this approach, a $NaMgF_3$–NaF eutectic is grown by directional solidification using the Bridgman technique. The NaF phase in the eutectic can then be leached in water to obtain a porous $NaMgF_3$ crystal with around 53% porosity. The size of the pores can be

* Corresponding author.
E-mail address: jrr@us.es (J. Ramírez-Rico).

0955-2219/$ – see front matter © 2008 Elsevier Ltd. All rights reserved.
doi:10.1016/j.jeurceramsoc.2008.04.002

modified by selecting appropriate growth conditions, but the porosity remains constant as it is equal to the volume fraction of the sacrificial phase, NaF in this case.

Neighborite ($NaMgF_3$) was discovered in 1961[15] and since then has been studied mainly for its interest as a low-pressure analogue of $MgSiO_3$[16–18] and for its ionic conduction properties.[19] It is an orthorhombic (*Pnma*) perovskite at room temperature and experiences a phase transition at 760 °C becoming cubic (*Pm*3*m*).[19–21] It melts at 1030 °C.[22] To the best of our knowledge, no data on the mechanical behavior of $NaMgF_3$ exists in the literature. In this paper we study both strength and creep in compression for porous $NaMgF_3$ fabricated from a eutectic at different growth rates, as reported in Ref. 14.

2. Experimental

2.1. Fabrication

Porous $NaMgF_3$ cylinders of about 1 cm^2 section were fabricated using a method previously described.[14] In brief, NaF 99% and MgF_2 99.9% purity powders supplied by Aldrich were dried and mechanically mixed in the proportions described in Ref. 23, of 70.7 wt.% NaF. The resulting powder was directionally solidified using the Bridgman method in a vitreous graphite crucible, in a dry Ar atmosphere. Growth rates of 8, 10 and 15 mm/h were used. The resulting $NaMgF_3$–NaF eutectics were submerged in distilled water and the NaF leached, leaving a porous $NaMgF_3$ crystal with 53% pore volume.[24]

2.2. Characterization

Samples of the $NaMgF_3$–NaF and porous $NaMgF_3$ were dry-milled in a WC ball mill for powder diffraction experiments using a Bruker D8 diffractometer. Microstructural observations were performed on both as fabricated and deformed samples by scanning electron microscopy (SEM) using a JEOL 6460LV microscope. Transverse and longitudinal sections were grinded, polished and carbon coated using conventional metallographic techniques. Image analysis was performed on SEM micrographs of transverse sections using Image Pro v4.0.

Compression tests were carried out in air at 30, 550, 650 and 750 °C at a constant strain rate of $2 \times 10^{-5}\ s^{-1}$ using a screw-driven universal testing machine (Microtest EM1/50/FR, Madrid, Spain) with a furnace mounted on its frame. Alumina pads were used between the alumina rods and the samples. Parallelepipeds measuring 3 mm × 3 mm × 5 mm were cut with their longest dimension parallel to the growth direction of the eutectic precursor and the sections in contact with the alumina pads were ground flat-parallel. Sample dimensions were chosen to follow a length/diameter <2.0 relation to minimize barrel deformation. Samples were tested up to failure.

Compressive creep tests were carried out in air at 650 and 750 °C for samples grown at 10 mm/h, using the same experimental setup with a load control module that maintains a constant uniaxial load with a precision of 0.1 N. Applied stresses ranged from 6 to 16 MPa.

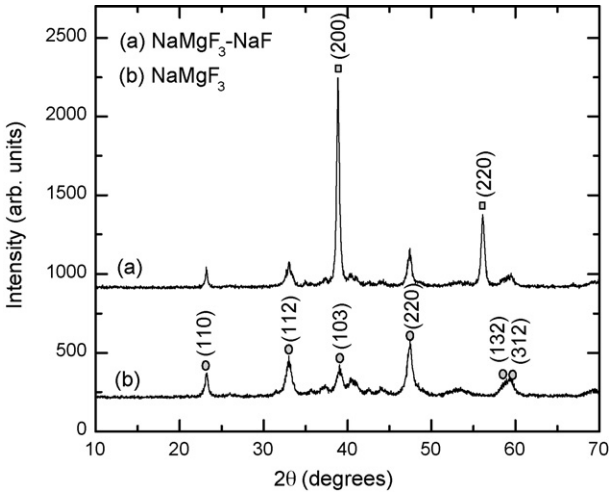

Fig. 1. X-ray diffractograms of (a) as-grown $NaMgF_3$–NaF eutectic and (b) porous $NaMgF_3$. Most intense reflections are marked (□) for NaF and (○) for $NaMgF_3$.

3. Results and discussion

3.1. Microstructure

Fig. 1 shows X-ray diffractograms for both the $NaMgF_3$–NaF eutectic and the porous $NaMgF_3$ obtained by leaching the eutectic in distilled water. All NaF was removed by leaching, which agrees with the connected nature of the porosity in $NaMgF_3$, as previously reported.[14,24]

The microstructure was similar to that reported previously.[14,23] It consists of eutectic grains with degenerated NaF lamellae that become pores after leaching (Fig. 2A) although in some areas it is fairly regular (Fig. 2B) and results in elongated, approximately cylindrical pores. The eutectic grains are crossed perpendicularly, so in adjacent grains the pores are aligned with their longest direction parallel and perpendicular to the growth direction. This is clearly seen in Fig. 2C. Fig. 2D shows a detail of the region between adjacent grains. The microstructure was similar for all the three growth rates. Pore size ranged from 4 to 8 μm and decreased when increasing growth rate, as reported.[14]

3.2. Compressive strength

The mechanical response was observed to be fairly independent of growth rate, with small differences in strength that become smaller as temperature is increased and were usually within the scatter of the data. This is to be expected since the porosity is independent of growth rate, as is fixed by the eutectic composition. Thus, the main microstructural difference between samples grown at different rates is a change in pore size, which follows a modified Jackson–Hunt law, as detailed in Ref. 14.

Fig. 3(left) shows the stress–strain curves for the samples grown at 8 mm/h, for all temperatures studied. The effect of plasticity is evident as temperature is increased. The samples studied at room temperature and 550 °C failed before any plastic

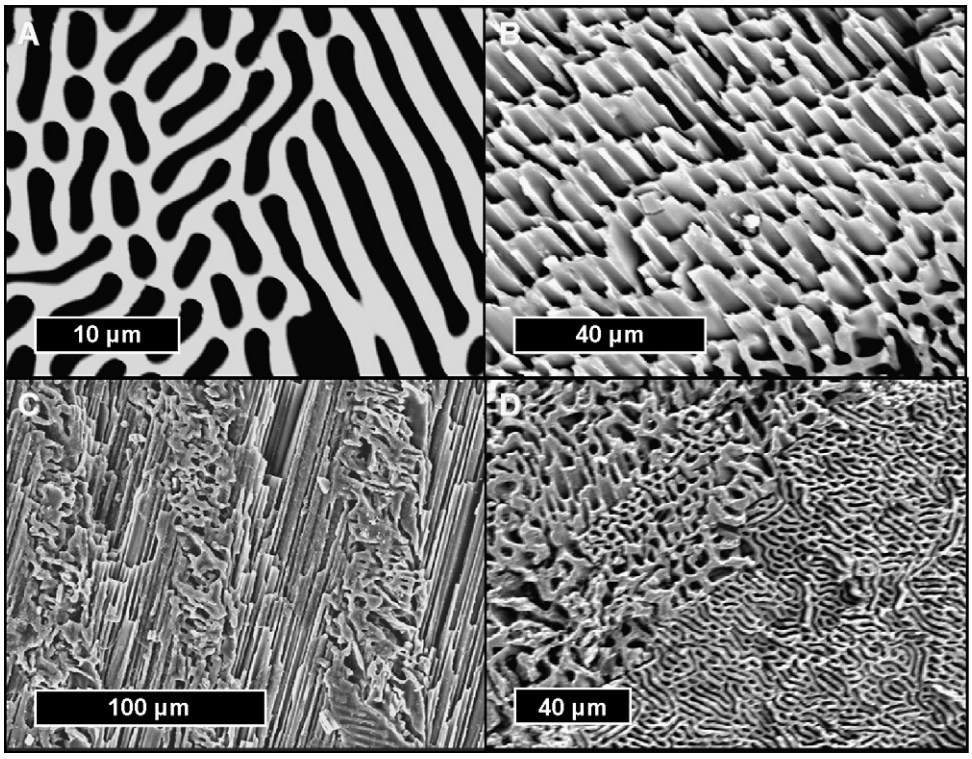

Fig. 2. SEM micrographs of porous $NaMgF_3$: (A) grown at 15 mm/h, transverse section; (B) grown at 15 mm/h, detail of a transverse section, fracture surface; (C) grown at 10 mm/h, longitudinal section; (D) grown at 8 mm/h transverse section.

deformation was observed, whereas the samples studied at 650 and 750 °C show extensive plasticity. The results of the compression experiments are summarized in Fig. 3(right). Differences in strength for different growth rates can be observed to decrease as temperature is increased. The difference in elastic modulus (see Fig. 3 and below) between room temperature and 550 °C produces a more uniform distribution of stress at 550 °C, being the stresses more localized at room temperatures. This explains why samples deformed at 550 °C were crushed after deformation, whereas samples studied at room temperature broke into a few chips. Most of the samples studied at room temperature remained intact. This explains why their strength was significantly lower than the strength at 550 °C.

The microstructure of the deformed specimens is shown in Fig. 4. No significant buckling was observed at the strains reached in our experiments. The cracks in the material were observed to start in the interface between perpendicularly aligned eutectic grains (Fig. 4, left) and then propagate across the grains (Fig. 4, right). This was observed at all temperatures. To rationalize these results the effects of pore alignment must be taken into account. It has been shown[25–27] that the physical properties of a porous material can be described as a function of the properties of the bulk material, taking into account the minimum solid area (MSA) of the porous structure, that is, the minimum area of solid material that can be found in any plane perpendicular to the excitation, in this case the applied stress. If we

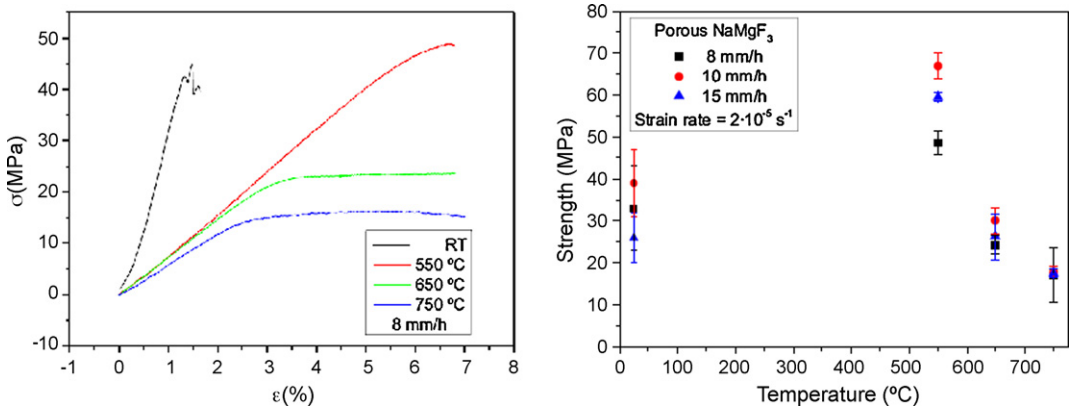

Fig. 3. Compression experiments. (Left) Stress–strain curves for a sample grown at 8 mm/h and studied at different temperatures. (Right) Strength (maximum stress) as a function of temperature for all growth conditions studied.

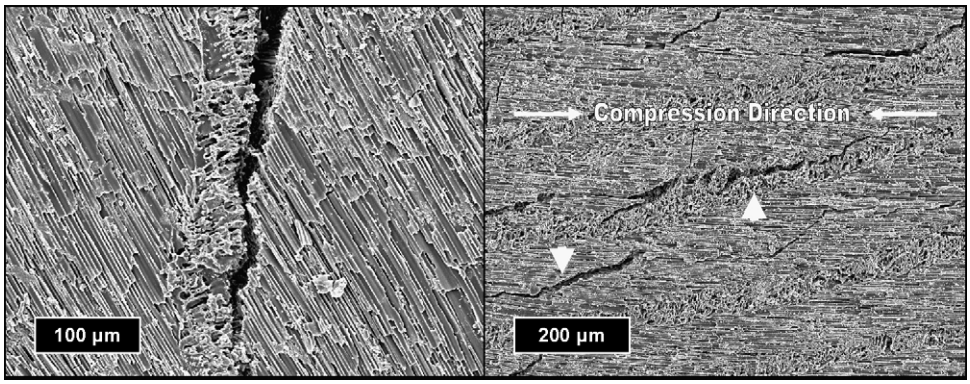

Fig. 4. Crack distribution in porous $NaMgF_3$ grown at 15 mm/h after compression at (left) 750 °C and (right) 550 °C.

consider a porous body with perfectly cylindrical pores arranged in a hexagonal lattice (Fig. 5), we can calculate the strength of the material in the directions parallel and perpendicular to the pores' axes as

$$\sigma_{||} = \sigma_{\text{bulk}} \left(1 - \frac{\sqrt{3}\pi}{6} \frac{a^2}{b^2}\right), \qquad \sigma_{\perp} = \sigma_{\text{bulk}} \left(1 - \frac{a^2}{b^2}\right) \quad (1)$$

where σ_{bulk} is the strength of the bulk material, a the pore radius and b is the distance between the axes of nearest neighboring pores. We can see that the relative strength of eutectic grains with their pores aligned with the compression direction is higher than the strength of the grains aligned perpendicular. Moreover, stiffness is expected to follow the same trend as in Eq. (1). Therefore, the effective stress at both sides of a eutectic grain boundary is expected to be different, thus creating a shear stress along the boundary that is responsible for crack initiation.

The fact that strength differences become smaller at higher temperatures suggests that they can be attributed to stress concentration effects. As has been shown,[28,29] the strength of a porous material with aligned pores can be described as a function of porosity, following:

$$\sigma = \sigma_{\text{bulk}}(1 - P)^k \quad (2)$$

where P is the porosity fraction and k is a constant defined as the ratio of maximum to applied stress around a pore, and depends only on pore shape. For the case of cylindrical pores in the parallel direction, it is found that $k = 1$, because no stress concentration effects are present. In the case of elliptical pores with semi axes a and b perpendicular and parallel to the applied stress, for compression in the direction perpendicular to the pores, it is given by

$$k = 1 + 2\frac{a}{b} \quad (3)$$

Here $k = 3$. Since $P < 1$, the strength perpendicular to the pores is smaller to that parallel to the pores, in agreement with the previous discussion. The differences in strength for different growth rates could be explained by a difference in the fraction of eutectic grains aligned perpendicular to the growth direction. As can be deduced from Eq. (2), as the volume fraction of perpendicular grains increases, the observed strength must decrease.

Since the elastic modulus of a porous material should follow the same trend as the fracture strength, we have calculated it from the strain–stress curves. First we performed a series of compression tests at the same conditions as the deformation experiments but without sample. We could then estimate the testing machine deformation as a function of applied load and subtract its influence. Then, the elastic modulus was calculated as the maximum slope of the strain–stress curves in the elastic region. We acknowledge that this has several drawbacks, and do not claim the results to be accurate or useful other that for inter-sample comparisons under the same experimental conditions (machine, furnace, load bearing rods, etc.). Fig. 6 shows a plot of the elastic modulus vs. temperature, calculated as described above. It can be seen that the same general trend as in the case of compressive strength is followed. Both modulus and strength are higher for samples grown at 8 mm/h than for samples grown at 10 mm/h. The case of 15 mm/h growth rate is somewhat different, as both strength and modulus data show much higher scatter. It is possible that the microstructure of samples grown at 15 mm/h is less regular due to the high-growth rate. This lack of regularity is responsible for this scatter (see Fig. 2).

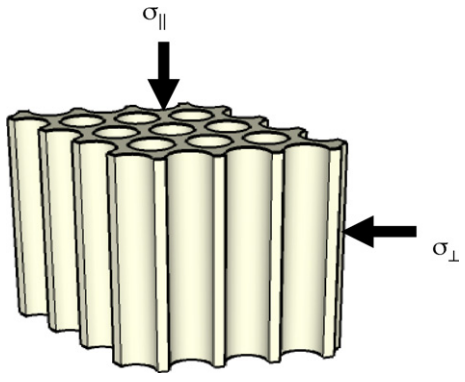

Fig. 5. Geometry of aligned cylindrical pores and definition of parallel and perpendicular directions.

3.3. Creep experiments

No steady state was reached during creep experiments for the stresses and temperatures studied. Instead, the time vs. strain curves showed a series of stair-like steps that involve brief

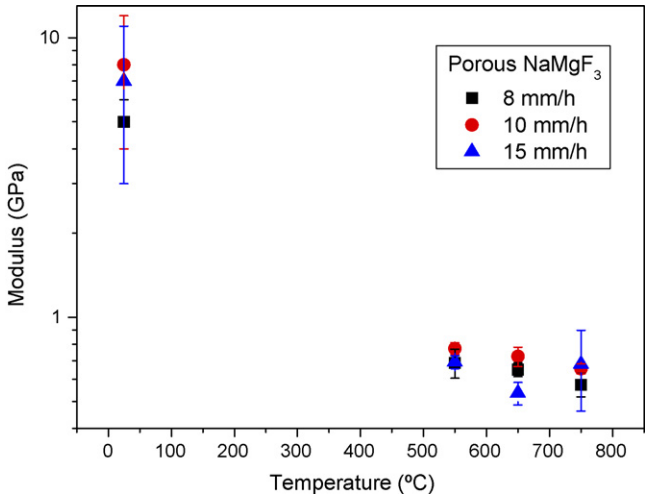

Fig. 6. Elastic modulus obtained from the strain–stress curves as discussed in the text. Semi-logarithmic scale is used for ease of view.

accelerations. This effects lead to a certain oscillation in the strain rate with time, as can be seen in Fig. 7. This behavior was observed in all stresses and temperatures studied, although it was more evident in some cases than others.

It has been shown that for cellular materials the creep rate can be described using the same parameters n and Q that describe creep in the bulk material[30] because the creep rate is controlled by the bending of material struts perpendicular to the applied stress, while those parallel remain essentially rigid. In these conditions, and assuming a cubic array of struts, the creep rate is

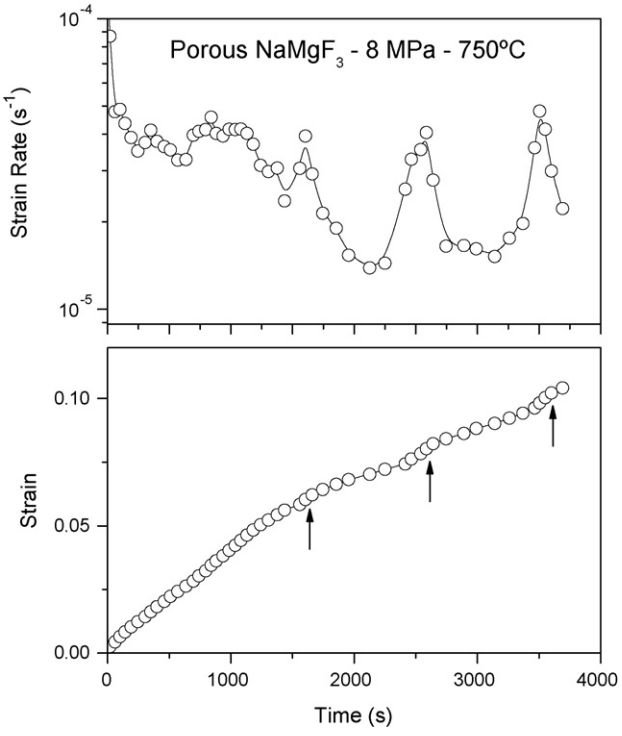

Fig. 7. Strain and strain rate vs. time for porous $NaMgF_3$ crept at 750 °C with a stress of 8 MPa. The strain showed certain stair-like steps which are marked by arrows. The solid line plotted is included only as a visual aid and does not correspond to any particular fit of the data.

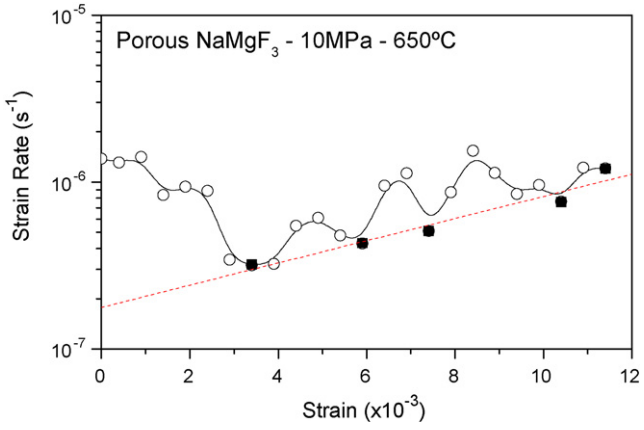

Fig. 8. Strain rate vs. time for porous $NaMgF_3$ crept at 650 °C and 10 MPa. The strain rate oscillates through a series of ascending minima. Black dots represent minima in the creep data. The solid and dashed lines plotted are included only as a visual aid and does not correspond to any particular fit of the data.

described by

$$\dot{\varepsilon} = A\frac{0.6}{n+2}\left(\frac{1.7(2n+1)}{n}\right)\sigma^n\rho^{-(3n+1)/2}\exp\left(-\frac{Q}{RT}\right) \quad (4)$$

where ρ is the relative density of the material, σ the uniaxial applied stress and Q and n are the activation energy and the stress exponent of the bulk material, respectively. Although this model has been successfully applied in the past to explain the observed creep rates in metallic foams,[31,32] it does not take into the account the possibility of strut cracking as strain progresses. The apparition of creep damage during the experiments, in the form of strut-breaking cracks, would cause the strain rate to increase as the number of load bearing struts decrease.

Fig. 8 shows the strain rate vs. strain relation for a porous $NaMgF_3$ sample crept at 650 °C and 10 MPa. It can be observed that the strain rate oscillates passing through a series of increasing minima. We can explain this behavior assuming that each acceleration step corresponds to the breakage of a group of struts, which decrease the effective load-bearing area or MSA in the material. As struts crack there is an increase in strain rate that is followed by stress redistribution among the remaining solid area, which slows down the creep until a new equilibrium rate is reached. This rate must, however, be higher than the previous one because the effective load bearing area is smaller, thus causing the observed effects

As has been shown, the strain rate depends on strain in a way that it is not possible to define a steady-state creep rate. If stress changes are performed during the creep experiments, the minimum creep rate observed for the new value of the stress after a stress jump will not be the same as the value one would observe for a fresh test specimen. Therefore it makes no sense to describe creep in the classical way using Eq. (4). Instead we have chosen to calculate the average strain rate over a strain range of 0.5% for samples crept at 650 °C and 1% for samples crept at 750 °C. These results are included in Fig. 9. It should be kept in mind that the reported values of the stress exponent n resulting from the linear fits in the creep rate vs. stress plot have no physical meaning because the absence of

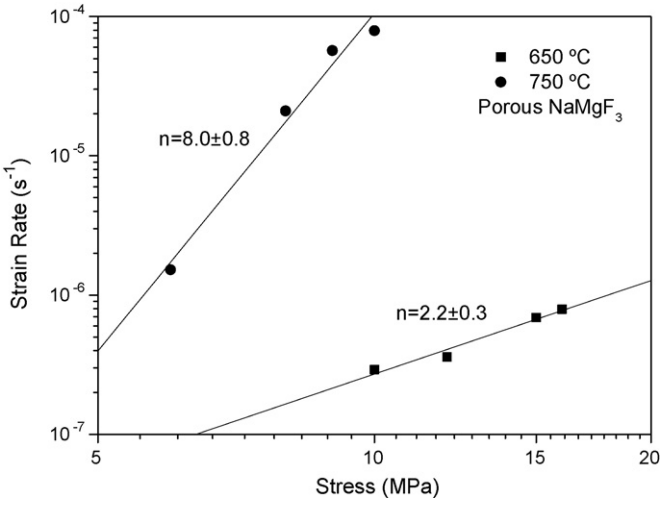

Fig. 9. Average creep rate at 650 and 750 °C. See text for details.

steady state creep, and are included only for visual comparison.

4. Conclusions

We have successfully fabricated $NaMgF_3$ porous materials with aligned pores starting from a $NaMgF_3$–NaF eutectic grown by the Bridgman technique. The microstructure is that of a degenerated eutectic with 53% connected porosity, and is fairly independent of growth rate. In consequence, the mechanical properties are also independent on growth rate, with small variations that are due to small differences in pore size and the presence of eutectic grains. In general, these differences can be explained using a MSA model. Both compressive strength and elastic modulus follow the same trend with respect to growth rate for samples grown at 8 and 10 mm/h, while those grown at 15 mm/h show significant scatter. No steady–state creep was observed, and the strain rate was found to oscillate passing through a series of ascending minima. This acceleration is attributed to damage propagation. Therefore, data cannot be fitted using the classic Norton equation.

Acknowledgements

This work was supported by the Spanish Ministry of Science and Technology through Grant MAT 2006-13005-C03-01. The authors are grateful to the CITIUS at the University of Seville for the use of their electron microscopy and X-Ray facilities. JR-R is grateful to the Junta de Andalucía for his pre-doctoral Grant.

References

1. Salvini, V. R., Sandurkov, B. A., Gunnewiek, F. K., Rosa, D. S. and Pandolfelli, V. C., Porous ceramics with tailored properties. *American Ceramic Society Bulletin*, 2007, **86**, 9401–9405.
2. Studart, A. R., Gonzenbach, U. T., Tervoort, E. and Gauckler, L. J., Processing routes to macroporous ceramics: a review. *Journal of the American Ceramic Society*, 2006, **89**, 1771–1789.
3. Isobe, T., Kameshima, Y., Nakajima, A., Okada, K. and Hotta, Y., Gas permeability and mechanical properties of porous alumina ceramics with unidirectionally aligned pores. *Journal of the European Ceramic Society*, 2007, **27**, 53–59.
4. Isobe, T., Tomita, T., Kameshima, Y., Nakajima, A. and Okada, K., Preparation and properties of porous alumina ceramics with oriented cylindrical pores produced by an extrusion method. *Journal of the European Ceramic Society*, 2006, **26**, 957–960.
5. Kaul, V. S., Faber, K. T., Sepulveda, R., de Arellano-López, A. R. and Martínez-Fernández, J., Precursor selection and its role in the mechanical properties of porous SiC derived from wood. *Materials Science and Engineering A: Structural Materials Properties Microstructure and Processing*, 2006, **428**, 225–232.
6. Llorca, J. and Orera, V. M., Directionally solidified eutectic ceramic oxides. *Progress in Materials Science*, 2006, **51**, 711–809.
7. Ramírez-Rico, J., Lopez-Robledo, M. J., de Arellano-López, A. R., Martínez-Fernández, J. and Sayir, A., Fabrication and microstructure of directionally solidified $SrCe_{1-x}Y_xO_{3-\delta}$ ($x = 0.1$, 0.2) high temperature proton conductors. *Journal of the European Ceramic Society*, 2006, **26**, 3705–3710.
8. Lopez-Robledo, M. J., Ramírez-Rico, J., Martínez-Fernández, J., de Arellano-López, A. R. and Sayir, A., Microstructure and creep behaviour of high temperature proton conducting perovskites. *Boletin De La Sociedad Espanola De Ceramica Y Vidrio*, 2005, **44**, 347–351.
9. Laguna-Bercero, M. A. and Larrea, A., YSZ-Induced crystallographic reorientation of Ni particles in Ni-YSZ cermets. *Journal of the American Ceramic Society*, 2007, **90**, 2954–2960.
10. Laguna-Bercero, M. A., Larrea, A., Merino, R. I., Peña, J. I. and Orera, V. M., Stability of channeled Ni-YSZ cermets produced from self-assembled NiO-YSZ directionally solidified eutectics. *Journal of the American Ceramic Society*, 2005, **88**, 3215–3217.
11. Laguna-Bercero, M. A., Larrea, A., Peña, J. I., Merino, R. I. and Orera, V. M., Structured porous Ni- and Co-YSZ cermets fabricated from directionally solidified eutectic composites. *Journal of the European Ceramic Society*, 2005, **25**, 1455–1462.
12. Orera, V. M. and Larrea, A., NaCl-assisted growth of micrometer-wide long single crystalline fluoride fibres. *Optical Materials*, 2005, **27**, 1726–1729.
13. Larrea, A., Contreras, L., Merino, R. I., Llorca, J. and Orera, V. M., Microstructure and physical properties of CaF_2–MgO eutectics produced by the Bridgman method. *Journal of Materials Research*, 2000, **15**, 1314–1319.
14. Larrea, A. and Orera, V. M., Porous crystal structures obtained from directionally solidified eutectic precursors. *Journal of Crystal Growth*, 2007, **300**, 387–393.
15. Chao, E. C. T., Evans, H. T., Skinner, B. J. and Milton, C., Neighborite, $NaMgF_3$, a new mineral from the Green River Formation, South Ouray, Utah. *American Mineralogist*, 1961, **46**, 379–393.
16. Okeeffe, M. and Bovin, J. O., Solid electrolyte behavior of $NaMgF_3$—geophysical implications. *Science*, 1979, **206**, 599–600.
17. Zhao, Y. S., Weidner, D. J., Ko, J. D., Leinenweber, K., Liu, X., Li, B. S. *et al.*, Perovskite at high *P–T* conditions—an in-situ synchrotron X-ray-diffraction study of $NaMgF_3$ perovskite. *Journal of Geophysical Research: Solid Earth*, 1994, **99**, 2871–2885.
18. Umemoto, K., Wentzcovitch, R. M., Weidner, D. J. and Parise, J. B., $NaMgF_3$: a low-pressure analog of $MgSiO_3$. *Geophysical Research Letters*, 2006, **33**.
19. Andersen, N. H., Kjems, J. K. and Hayes, W., Ionic-conductivity of the perovskites $NaMgF_3$, $KMgF_3$ and $NaZnF_3$ at high-temperatures. *Solid State Ionics*, 1985, **17**, 143–145.
20. Topor, L., Navrotsky, A., Zhao, Y. and Weidner, D. J., Thermochemistry of fluoride perovskites: heat capacity, enthalpy of formation, and phase transition of $NaMgF_3$. *Journal of Solid State Chemistry*, 1997, **132**, 131–138.
21. Yoshiasa, A., Sakamoto, D., Okudera, H., Ohkawa, M. and Ota, K., Phase relation of $Na_{1-x}K_xMgF_3$ ($1 \leq x \leq 1$) perovskite-type solid-solutions. *Materials Research Bulletin*, 2003, **38**, 421–427.
22. Adamkovicova, K., Fellner, P., Kosa, L., Nerad, I., Proks, I. and Strecko, J., Determination of the enthalpy of fusion of $NaMgF_3$ and $KMgF_3$. *Thermochimica Acta*, 1994, **242**, 23–26.
23. Bright, M. W. A. and Lewis, M. H., Eutectic solidification in the NaF–MgF_2 system. *Journal of Materials Science*, 1971, **6**, 1246–1253.

24. Merino, R. I., Peña, J. I., Larrea, A., de la Fuente, G. and Orera, V. M., *Recent Research and Development in Materials Science*, 2003, **4**, 1.
25. Rice, R. W., *Porosity of Ceramics*. Marcel Dekker Inc., New York, 1998.
26. Rice, R. W., Comparison of physical property porosity behaviour with minimum solid area models. *Journal of Materials Science*, 1996, **31**, 1509–1528.
27. Rice, R. W., Evaluation and extension of physical property–porosity models based on minimum solid area. *Journal of Materials Science*, 1996, **31**, 102–118.
28. Nakajima, H., Fabrication, properties and application of porous metals with directional pores. *Progress in Materials Science*, 2007, **52**, 1091–1173.
29. Boccaccini, A. R., Influence of stress concentrations on the mechanical property–porosity correlation in porous materials. *Journal of Materials Science Letters*, 1998, **17**, 1273–1275.
30. Andrews, E. W., Gibson, L. J. and Ashby, M. F., The creep of cellular solids. *Acta Materialia*, 1999, **47**, 2853–2863.
31. Andrews, E., Sanders, W. and Gibson, L. J., Compressive and tensile behaviour of aluminum foams. *Materials Science and Engineering A: Structural Materials Properties Microstructure and Processing*, 1999, **270**, 113–124.
32. Andrews, E. W., Huang, J. S. and Gibson, L. J., Creep behavior of a closed-cell aluminum foam. *Acta Materialia*, 1999, **47**, 2927–2935.